J Appl Electrochem (2014) 44:1069–1074
DOI 10.1007/s10800-014-0716-9

RESEARCH ARTICLE

Facile microwave synthesis of $CoFe_2O_4$ spheres and their application as an anode for lithium-ion batteries

Sukeun Yoon

Received: 30 April 2014 / Accepted: 14 July 2014 / Published online: 17 August 2014

Abstract $CoFe_2O_4$ spheres were synthesized using a microwave-hydrothermal reaction and characterized by X-ray diffraction, electron microscopy, and electrochemical analysis. This simple synthesis method led to a uniform dispersion of nanosized building blocks in the spheres, which exhibit significantly improved cycling performance and rate capability in lithium cells. The excellent electrochemical performances of $CoFe_2O_4$ sphere are attributed to an increased lithium wetting property at the electrode–electrolyte interface, facile lithium-ion diffusion, and better alleviation of the structure pulverization during charge–discharge process.

Keywords Lithium-ion batteries · Anode · $CoFe_2O_4$ · Microwave-hydrothermal reaction

1 Introduction

Nanomaterials with various morphologies, such as nanowires, nanotubes, and nanoflowers, have attracted much attention in recent years because of their high surface to volume ratio, delocalization of carriers, excellent physical properties, and potential applications in a wide range of fields, including solar energy conversion, photocatalysis, photochromic devices, gas sensing, and energy storage [1–4]. In particular, there is extensive interest in utilizing one-, two-, and three-dimensional nanostructures to improve the performance of lithium-ion batteries. For example, tin oxide, titanium oxide, molybdenum oxide, iron oxide, and cobalt oxide anodes have theoretical capacities exceeding that of a graphite anode and have been studied for use in batteries operating at a relatively low potential [5–14]. Nanostructured materials with a large surface area can also accommodate the strain occurring during cycling and can provide easy access to the electrolyte, which shortens the diffusion pathway for electronic/ionic transport and improve the rate capability [15, 16]. In this regard, ternary transition metal oxides AB_2O_4 (where A and B are transition metals and the A and B-ions occupy the tetrahedral and octahedral sites in the cubic spinel structure, respectively) can be used as anode materials with high energy densities and better safe than graphite, because they operate at potentials well above that of Li^+/Li and show less surface reactivity with the electrolyte. Although the working potentials of AB_2O_4 are high for negative electrode materials, they are still electrochemically stabile in common electrolytes [17–25]. Various approaches have been developed for synthesizing of AB_2O_4, including hydro/solvothermal reactions, combustion, and sol–gel methods. For example, the microwave-assisted hydrothermal (MW-HT) method has recently been gaining popularity for the synthesis of nanomaterials, as it offers a clean, low-cost approach with a very short reaction time (few minutes) and high yield [26, 27]. Therefore, we herein present the facile MW-HT synthesis of $CoFe_2O_4$ spheres with stable capacity retention and enhanced rate capability for lithium batteries. In this facile MW-HT approach, $CoFe_2O_4$ spheres are synthesized without any surfactant within 25 min in an ethanol–water solution at 170 °C. When employed as anodes in lithium cells, the as-synthesized $CoFe_2O_4$ spheres exhibit a high reversible capacity of ~ 730 mAh g^{-1} with excellent cyclability and high-rate performance.

S. Yoon (✉)
Division of Advanced Materials Engineering, Kongju National University, Chungnam 330-717, Republic of Korea
e-mail: skyoon@kongju.ac.kr

2 Experimental

$CoFe_2O_4$ spheres were obtained by microwave-hydrothermal reaction without the use of any surfactants. In a typical experiment, 30 mmol urea ($(NH_2)_2CO$, >99 %, Alfa) was dissolved in distilled (DI) water and ethanol under mild stirring. Urea was added to control the rate of hydrolysis, since the ammonia produced by the hydrolysis of urea controls the pH of the reaction at temperatures higher than 80 °C. Then, 2 mmol cobalt chloride hexahydrate ($CoCl_2 \cdot 6H_2O$, >98 %, Alfa) and 4 mmol iron chloride hexahydrate ($FeCl_3 \cdot 6H_2O$, >97 %, Alfa) were added to the stirred mixture. The resulting transparent solution was transferred to quartz vessels in an Anton Paar microwave synthesis system (Synthos-3000) operated at 2.45 GHz and 600 W. The sample temperature was ramped to 170 °C and then maintained at that temperature for 25 min. After the MW-HT process, the resultant slurries were washed and filtered with DI water and then dried in a vacuum oven. The resultant powders were calcined at 500 °C in air.

The phase of the synthesized sample was analyzed using a Phillips X-ray diffractometer with Cu Kα radiation. The morphology, microstructure, and composition of the synthesized powders were examined using a Hitachi S-5500 scanning transmission electron microscope (STEM) and JEOL 2010F transmission electron microscope (TEM). The specific surface areas were evaluated with a Quantachrome analyzer based on the Brunauer–Emmett–Teller (BET) multipoint method and N_2 physisorption at 77 K. Adsorption–desorption isotherm measurements were used to determine the porosity and pore size distribution using the Barrett–Joyner–Halenda (BJH) method.

The electrodes for the electrochemical evaluation were prepared by mixing 70 wt% active material ($CoFe_2O_4$) powder, 15 wt% carbon black (Super P) as a conducting agent, and 15 wt% polyvinylidene fluoride (PVDF) dissolved in *N*-methylpyrrolidinone (NMP) as a binder to form a slurry that was coated on copper foil, pressed, and dried at 120 °C for 3 h under vacuum. The loading of active material ($CoFe_2O_4$) was 1.7–2.0 mg cm^{-2}. CR2032 coin cells were assembled in an Ar-filled glove box using Celgard polypropylene as a separator, lithium foil as the counter electrode, and 1 M $LiPF_6$ in ethylene carbonate (EC)/diethyl carbonate (DEC) (1:1 v/v) as the electrolyte. The charge–discharge experiments were performed galvanostatically at a constant current density of 100 mA g^{-1} of the active material within the voltage range of 0.005–3 V vs. Li^+/Li. To understand the evolution of the lithium diffusivity as a function of cell potential, the galvanostatic intermittent titration technique (GITT) was employed. A current pulse of 50 mA g^{-1} was applied for 5 min to measure the closed-circuit voltage (CCV) and then turned off for 10 min to obtain the quasi-open-circuit voltage (QOCV). Sequential current pulses were applied for both the discharge and charge periods within a voltage range of 0.005–3 V vs. Li^+/Li. The electrochemical impedance spectroscopic (EIS) analysis was performed with Solartron SI1260 equipment by applying a 10 mV signal in a frequency range of 10 kHz to 0.001 Hz. For the EIS measurements, a $CoFe_2O_4$ electrode with an active material content of 1.8 mg served as the working electrode and lithium foil served as the counter and reference electrodes. The impedance response was measured after different number of discharge–charge cycles (after 1 and 20 cycles) at 3 V vs. Li^+/Li.

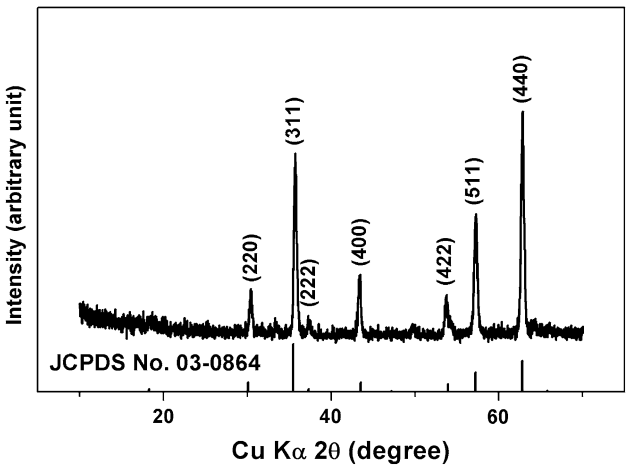

Fig. 1 XRD patterns of $CoFe_2O_4$ spheres

3 Results and discussion

The X-ray diffraction (XRD) patterns of the $CoFe_2O_4$ spheres are shown in Fig. 1. All reflections were marked on the XRD pattern and could be indexed to the $CoFe_2O_4$ phase ($Fd\bar{3}m$, JCPDS No. 03-0864). The diffraction peaks located at $2\theta = 33.1°$ and 49.6° were assigned to the Fe_2O_3 impurity.

The STEM images shown in Fig. 2 reveal an average particle size of ~1 μm and a homogeneous distribution of Fe, Co, and O in the $CoFe_2O_4$ sphere. The selected individual single sphere (Fig. 2c, d) clearly displays a rough surface. Figure 3 shows TEM images of $CoFe_2O_4$ spheres along with the corresponding fast Fourier transform (FFT) image over the selected region. It is clearly seen that the nanoparticles are uniformly dispersed throughout the whole sphere and that each nanoparticle has an average size of ~40 nm. The three-dimensional interconnected framework of the $CoFe_2O_4$ sphere is made up of these nanosized building-block particles. The FFT image shows a set of

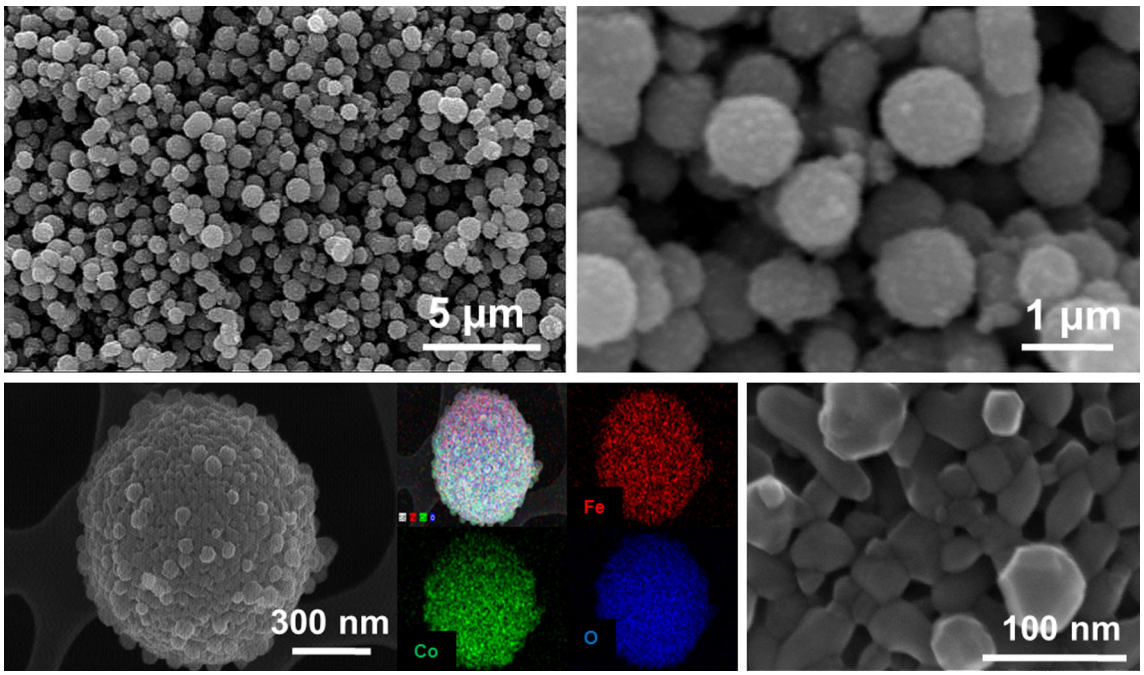

Fig. 2 SEM images of $CoFe_2O_4$ spheres at different magnification levels. The *colors* corresponding to each element (Co, Fe, O) are also shown. (Color figure online)

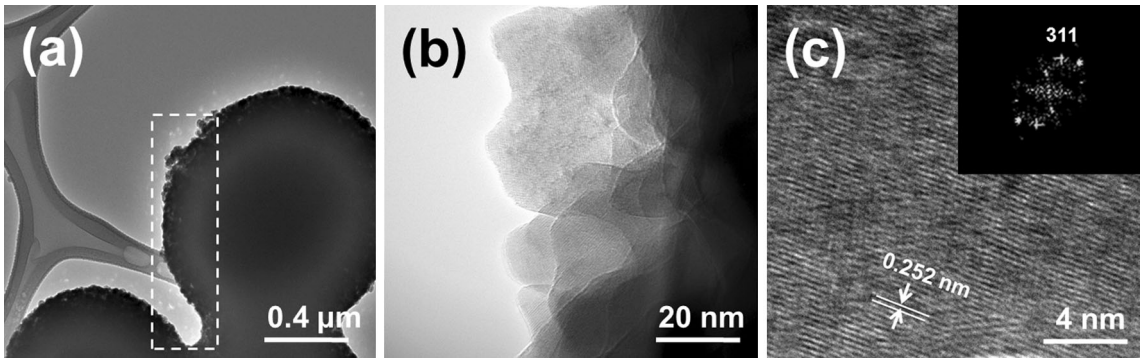

Fig. 3 **a** TEM and **b**, **c** HRTEM images of $CoFe_2O_4$ spheres. The *inset* in **c** is the fast Fourier transform (FFT) image over a selected region of the $CoFe_2O_4$ sphere

sharp spots corresponding to the (311) plane of the $CoFe_2O_4$ phase.

In order to confirm the changes in the surface area of the $CoFe_2O_4$ sphere, N_2 adsorption–desorption isotherm was carried out as shown in Fig. 4. The BET multipoint method was used to calculate the specific area. The BET surface area and total pore volume were 24.5 $m^2\ g^{-1}$ and 0.18 $cm^3\ g^{-1}$, respectively. The nitrogen adsorption–desorption isotherm exhibits a type IV isotherm with hysteresis loop, indicating the presence of mesopores [24]. BJH pore size distributions for the $CoFe_2O_4$ sphere demonstrates the presence of well-developed mesoporosity with narrow pore size distributions and an average pore diameter of 25 nm.

Figure 5 shows the first and second discharge–charge profiles and differential capacity plots (DCPs) of the $CoFe_2O_4$ spheres. The first discharge and charge capacities (Fig. 5a) are 1,224 and 930 mAh g^{-1}, respectively, implying an initial Coulombic efficiency of 76 %. The increasing specific capacity was caused by deeper lithium-ion insertion in $CoFe_2O_4$ or an undesirable side reaction with the electrolyte related with solid electrolyte interphase (SEI). The DCP in Fig. 5b shows feature characteristic of the voltage plateau during the first discharge process at ~0.82 V, which corresponds to the conversion reactions of Fe^{3+} and Co^{2+} to their metallic states and the formation of Li_2O and the irreversible reaction with electrolyte to form a SEI film. The voltage plateau is increased slightly to

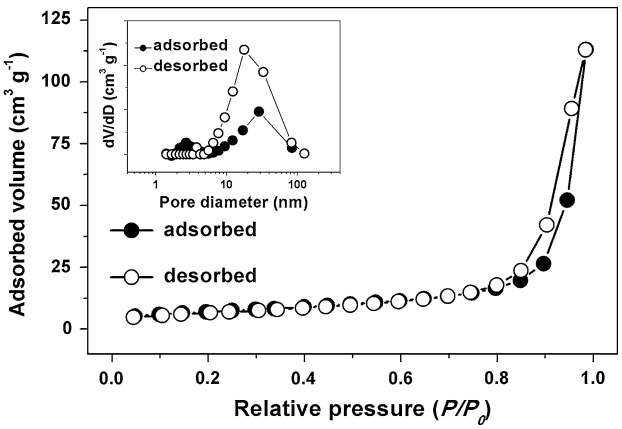

Fig. 4 Nitrogen adsorption–desorption isotherm and BJH pore size distribution plot (*inset*) of the $CoFe_2O_4$ sphere

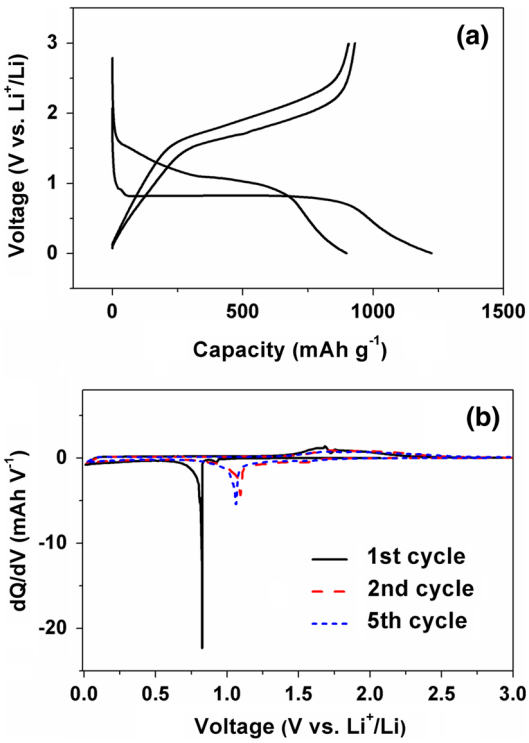

Fig. 5 **a** Discharge–charge profiles for the first and second cycles and **b** differential capacity plots (DCPs) for the first, second, and fifth cycles of $CoFe_2O_4$ spheres

$\sim$1.2 V after the first cycle, indicating reduction of Fe^{3+} and Co^{2+} to metallic Fe^0 and Co^0, respectively [19]. The main anodic peak at $\sim$1.75 V during the charge process is meanwhile ascribed to the reversible oxidation of the Fe^0 and Co^0 to Fe^{3+} and Co^{2+}, respectively. However, the integrated area and peak intensity during the cathodic and anodic process don't decrease almost in the subsequent scans, indicating the good capacity retention of the $CoFe_2O_4$ spheres electrode.

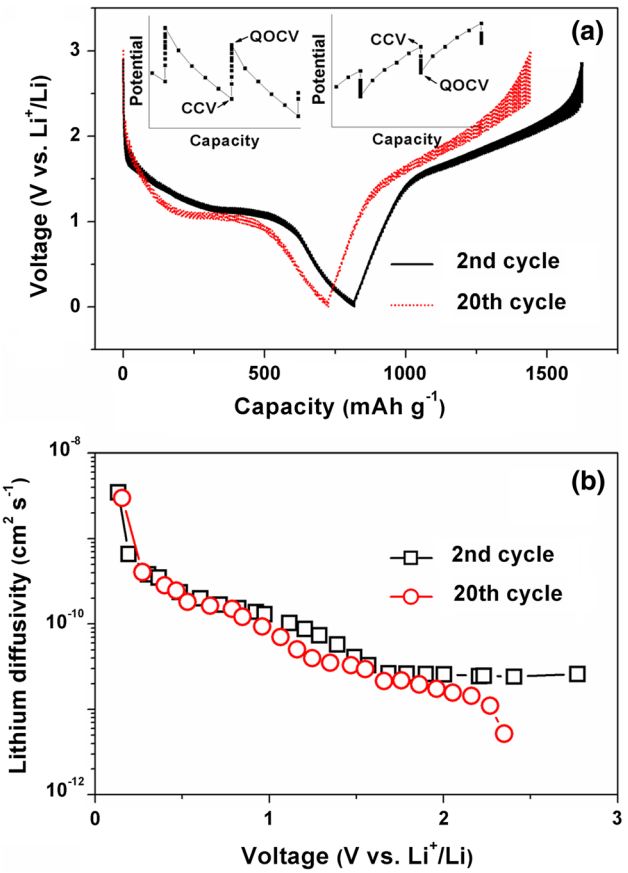

Fig. 6 **a** GITT voltage profiles and **b** lithium diffusivities of $CoFe_2O_4$ spheres as a function of the cell potential during the second and 20th cycles determined by GITT during Li deintercalation (*charging*)

The GITT was employed to investigate the evolution of the lithium diffusivity as a function of the cell potential, as shown in Fig. 6a. Weppner and Huggins [28] derived a simple expression for lithium diffusivity in the electrode, as given below:

$$D_{\mathrm{Li}} = \frac{4L^2}{\pi\tau}\left[\frac{\Delta E_s}{\Delta E_\tau}\right]^2,$$

where L is the electrode thickness, τ is the time interval of the current pulse (300 s), and ΔE_τ and ΔE_s are the voltage changes during the applied current pulse and the turned-off current pulse, respectively. The ideal density for the $CoFe_2O_4$ spheres was used in this equation. Figure 6b shows the lithium diffusivity of the $CoFe_2O_4$ spheres as a function of the cell potential during the charge process. The lithium diffusivity in the second cycle is between $\sim 3 \times 10^{-9}$ and $\sim 2 \times 10^{-11}$ cm^2 s^{-1}. It is also still high, $\sim 5 \times 10^{-12}$ cm^2 s^{-1}, after the 20th cycle, because there is little degradation of the $CoFe_2O_4$ spheres. This result suggests that the nanosized building blocks of the $CoFe_2O_4$ spheres can allow this material to tolerate the volume

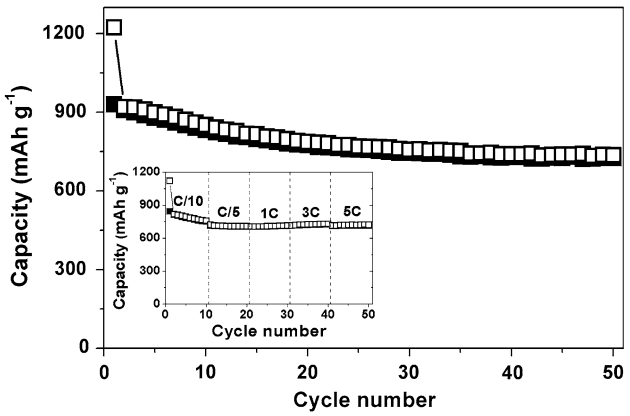

Fig. 7 Cycling performance of $CoFe_2O_4$ spheres. *Open* and *closed symbols* represent the discharge and charge capacity values, respectively. The *inset* shows the rate capability of the $CoFe_2O_4$ spheres

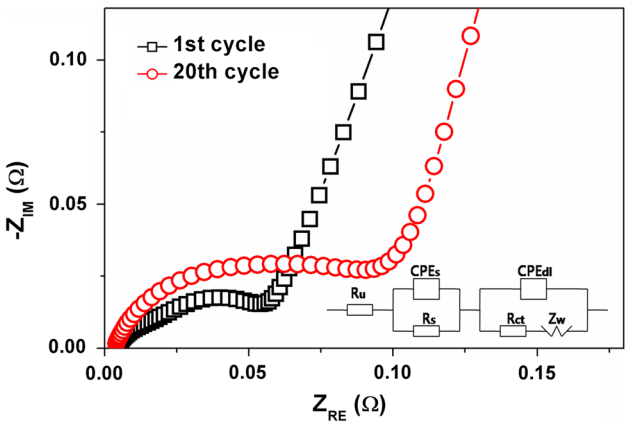

Fig. 8 Electrochemical impedance spectra (EIS) of $CoFe_2O_4$ spheres. The *inset* shows the equivalent circuit

expansion and contraction during the electrochemical cycling by maintaining good electrical contact.

Figure 7 shows the cyclability of $CoFe_2O_4$ spheres between 0.005 and 3 V at a constant current of 100 mA g^{-1} (C/10 rate). The $CoFe_2O_4$ spheres show good cyclability, and this good capacity retention is attributed to the good accommodation of structural changes and to the facile lithium diffusion during the lithium insertion processes, as described above. The inset graph shows the excellent rate capabilities of the $CoFe_2O_4$ spheres for C rates ranging from 0.1C to 5C. It should be noted that the spheres retain high capacities of $\sim$725 and 720 mAh g^{-1} at rates of 3C and 5C rates, respectively, with stable cycling.

In order to gain further insight into the electrochemical performance, EIS measurements were carried out at 3 V vs. Li^+/Li with $CoFe_2O_4$ sphere samples after the first cycle and 20th cycle. The EIS data were analyzed based on the equivalent circuit shown in Fig. 8 [29]. The EIS spectra for the $CoFe_2O_4$ spheres after the first and 20th cycles are composed of two semicircles and a line. The small diameter of the first semicircle in the high-frequency region is a measure of the surface layer resistance R_s, which is ascribed to lithium-ion diffusion through the surface layer. After the first and 20th cycles, the $CoFe_2O_4$ spheres show surface resistances of 0.023 and 0.06 Ω and charge transfer resistances of 0.065 and 0.105 Ω, respectively. The diameters of both the R_s and R_{ct} semicircles increase only slightly up to the 20th cycle, possibly because of the good electrical contact between the current collector and the particles due to the nanosized building blocks.

4 Conclusions

$CoFe_2O_4$ spheres were synthesized using a microwave-hydrothermal process and post-synthesis calcination and were investigated as an anode material for lithium-ion batteries. The XRD, STEM, TEM, and BET data reveal nanosized building blocks uniformly dispersed in the spheres and the existence of a large surface area. The $CoFe_2O_4$ spheres exhibit excellent electrochemical performance with a good rate capability and a capacity of more than 730 mAh g^{-1} after 50 cycles. The nanosized building blocks of the $CoFe_2O_4$ spheres, with their low crystallite size and large surface area, furnish good electrical contact, better accommodation of structural changes, and facile lithium diffusion during the lithium insertion processes, thus providing good electrochemical performance.

Acknowledgments This work was supported by the Korea Institute of Energy Research (No. GP2012-0024-03).

References

1. Gudiksen MS, Lauhon LJ, Wang J, Smith DC, Lieber CM (2002) Growth of nanowire superlattice structures for nanoscale photonics and electronics. Nature 415:617–620
2. Pacholski C, Kornowski A, Weller H (2002) Self-assembly of ZnO: from nanodots to nanorods. Angew Chem Int Ed 41:1188–1191
3. Redl FX, Cho KS, Murray CB, O'Brien S (2003) Three-dimensional binary superlattices of magnetic nanocrystals and semiconductor quantum dots. Nature 423:968–971
4. Bruce PG, Scrosati B, Tarascon JM (2008) Nanomaterials for rechargeable lithium batteries. Angew Chem Int Ed 47:2930–2946
5. Yang LC, Gao QS, Zhang YH, Tang Y, Wu YP (2008) Tremella-like molybdenum dioxide consisting of nanosheets as an anode material for lithium ion battery. Electrochem Commun 10:118–122
6. Xia XH, Tu JP, Xiang JY, Huang XH, Wang XL, Zhao XB (2010) Hierarchical porous cobalt oxide array films prepared by electrodeposition through polystyrene sphere template and their applications for lithium ion batteries. J Power Sources 195:2014–2022

7. Li CC, Li QH, Chen LB, Wang TH (2011) Topochemical synthesis of cobalt oxide nanowire arrays for high performance binderless lithium ion batteries. J Mater Chem 21:11867–11872
8. Yoon S, Manthiram A (2011) Hollow core-shell mesoporous TiO_2 spheres for lithium ion storage. J Phys Chem C 115:9410–9416
9. Zhu X, Zhu Y, Murali S, Stoller MD, Ruoff RS (2011) Reduced graphene oxide/tin oxide composite as an enhanced anode material for lithium ion batteries prepared by homogenous coprecipitation. J Power Sources 196:6473–6477
10. Yim CH, Baranova EA, Courtel FM, Abu-Lebdeh Y, Davidson IJ (2011) Synthesis and characterization of macroporous tin oxide composite as an anode material for Li-ion batteries. J Power Sources 196:9731–9736
11. Li MY, Wang Y, Liu CL, Gao H, Dong WS (2012) Iron oxide/carbon microsphere lithium-ion battery electrode with high capacity and good cycling stability. Electrochim Acta 67:187–193
12. Ding Y, Li J, Zhao Y, Guan L (2012) Direct synthesis of iron oxide nanoparticles on an iron current collector as binder-free anode materials for lithium-ion batteries. Mater Lett 81:105–107
13. Ryu MH, Jung KN, Shin KH, Han KS, Yoon S (2013) High performance N-doped mesoporous carbon decorated TiO_2 nanofibers as anode materials for lithium-ion batteries. J Phys Chem C 117:8092–8098
14. Choi SH, Kang YC (2014) Crumpled graphene-molybdenum oxide composite powders: preparation and application in lithium-ion batteries. ChemSusChem 7:523–528
15. Davis ME (2002) Ordered porous materials for emerging applications. Nature 417:813–821
16. Goltner CG, Smarsly B, Berton B, Antonietti M (2001) On the microporous nature of mesoporous molecular sieves. Chem Mater 13:1617–1624
17. Lavela P, Tirado JL (2007) $NiFe_2O_4$ synthesized by sol-gel procedures for their use as anode materials for Li ion batteries. J Power Sources 172:379–387
18. Sharma Y, Sharma N, Subba Rao GV, Chowdari BVR (2008) Studies on spinel cobaltites, $FeCo_2O_4$ and $MgCo_2O_4$ as anodes for Li-ion batteries. Solid State Ionics 179:587–597
19. Li ZH, Zhao TP, Zhan XY, Gao DS, Xiao QZ, Lei GT (2010) High capacity three-dimensional ordered macroporous $CoFe_2O_4$ as anode material for lithium ion batteries. Electrochim Acta 55:4594–4598
20. Liu S, Xie J, Fang C, Cao G, Zhu T, Zhao X (2012) Self-assembly of a $CoFe_2O_4$/graphene sandwich by a controllable and general route: towards a high-performance anode for Li-ion batteries. J Mater Chem 22:19738–19743
21. Zhang Z, Wang Y, Zhang M, Tan Q, Lv X, Zhong Z, Su F (2013) Mesoporous $CoFe_2O_4$ nanospheres cross-linked by carbon nanotubes as high-performance anodes for lithium-ion batteries. J Mater Chem A 1:7444–7450
22. Lee SH, Yu SH, Lee JE, Jin A, Lee DJ, Lee N, Jo H, Shin K, Ahn TY, Kim YW, Choe H, Sung YE, Hyeon T (2013) Self-assembled Fe_3O_4 nanoparticle clusters as high-performance anodes for lithium ion batteries via geometric confinement. Nano Lett 13:4249–4256
23. Lei C, Han F, Sun Q, Li WC, Lu AH (2014) Confined nanospace pyrolysis for the fabrication of coaxial Fe_3O_4@C hollow particles with a penetrated mesochannel as a superior anode for Li-ion batteries. Chem Eur J 20:139–145
24. Xiong QQ, Tu JP, Shi SJ, Liu XY, Wang XL, Gu CD (2014) Ascorbic acid-assisted synthesis of cobalt ferrite ($CoFe_2O_4$) hierarchical flower-like microspheres with enhanced lithium storage properties. J Power Sources 256:153–159
25. Fu X, Chen D, Wang M, Yang Y, Wu Q, Ma J, Zhao X (2014) Synthesis of porous $CoFe_2O_4$ octahedral structures and studies on electrochemical Li storage behavior. Electrochim Acta 116:164–169
26. Zhu G, Pan L, Xu T, Sun Z (2011) One-step synthesis of CdS sensitized TiO_2 photoanodes for quantum dot-sensitized solar cells by microwave assisted chemical bath deposition method. ACS Appl Mater Interfaces 3:1472–1478
27. Shi Y, Chou SL, Wang JZ, Wexler D, Li HJ, Liu HK, Wu Y (2012) Graphene wrapped $LiFePO_4$/C composites as cathode materials for Li-ion batteries with enhanced rate capability. J Mater Chem 22:16465–16470
28. Weppner W, Huggins RA (1977) Determination of the kinetic parameters of mixed-conducting electrodes and application to the system Li_3Sb. J Electrochem Soc 124:1569–1578
29. Yoon S, Manthiram A (2009) Sb–MO_x–C (M = Al, Ti, or Mo) nanocomposite anodes for lithium-ion batteries. Chem Mater 21:3898–3904